

A redox switch regulates the assembly and anti-CRISPR activity of AcrIIIC1

Received: 7 April 2022

Accepted: 25 October 2022

Published online: 18 November 2022



Yanan Zhao^{1,5}, Jiaojiao Hu^{2,5}, Shan-Shan Yang^{3,5}, Jing Zhong¹, Jianping Liu², Shuo Wang⁴, Yuzhuo Jiao¹, Fang Jiang¹, Ruiyang Zhai¹, Bingnan Ren¹, Hua Cong¹, Yuwei Zhu⁴, Fengtong Han¹, Jixian Zhang¹, Yue Xu¹, Zhiwei Huang⁴, Shengnan Zhang² & Fan Yang¹✉

Anti-CRISPRs (Acrs) are natural inhibitors of bacteria's CRISPR-Cas systems, and have been developed as a safeguard to reduce the off-target effects of CRISPR gene-editing technology. Acrs can directly bind to CRISPR-Cas complexes and inhibit their activities. However, whether this process is under regulation in diverse eukaryotic cellular environments is poorly understood. In this work, we report the discovery of a redox switch for *NmeAcrIIIC1*, which regulates *NmeAcrIIIC1*'s monomer-dimer interconversion and inhibitory activity on Cas9. Further structural studies reveal that a pair of conserved cysteines mediates the formation of inactive *NmeAcrIIIC1* dimer and directs the redox cycle. The redox switch also applies to the other two AcrIIIC1 orthologs. Moreover, by replacing the redox-sensitive cysteines, we generated a robust AcrIIIC1 variant that maintains potent inhibitory activity under various redox conditions. Our results reveal a redox-dependent regulation mechanism of Acr, and shed light on the design of superior Acr for CRISPR-Cas systems.

Over the past decade, the Clustered Regularly Interspaced Short Palindromic Repeat-associated nuclease Cas (CRISPR-Cas) systems have emerged as the most preferred genome-engineering tool in living eukaryotic cells, in both research and therapeutic applications. One of the many advantages that CRISPR-Cas offers over other genome-editing techniques, such as zinc finger nucleases (ZFNs) and transcription activator-like effector nucleases (TALENs), is its ease of programmability¹. Yet, in addition to programmability, reliability is a greater consideration when evaluating genome-editing tools, especially for applications in human cells. This is because all genome-editing tools, including CRISPR-Cas9, bear potentially deleterious cleavages of non-targeted sites (off-target effects)^{2,3}. Against this background, anti-CRISPR (Acr) proteins have drawn much attention ever since their identification, due to their potential applications in precise control of gene

editing and reduction of off-target effects of the CRISPR technology^{4–7}.

Acrs are typically small proteins (~80–150 aa) evolved by phage as a self-defense mechanism against the CRISPR-Cas systems. They can inactivate the CRISPR-Cas systems by inhibiting target DNA binding or cleavage, or in rare cases by preventing proper CRISPR-Cas complex assembly, like type II inhibitor AcrIIIC2^{6,8–12}. Several Acrs have shown prominent activities of regulating gene-editing events in different cell types, such as two *Spy*Cas9 inhibitors AcrIIA2 and AcrIIA4, and two *Nme*Cas9 inhibitors AcrIIC1 and AcrIIC3^{6,8,13}. Among the different Acr proteins characterized so far, AcrIIC1, a broad-spectrum inhibitor against diverse type II-C Cas9 orthologs, is one of the most promising engineering candidates to target the desired Cas9^{8,14}. Structural studies show that AcrIIC1 can directly bind to the conserved HNH nuclease domain of Cas9 to abolish its DNA cleavage activity¹⁴. Recently, a

¹School of Life Science and Technology, Harbin Institute of Technology, Harbin 150080, China. ²Interdisciplinary Research Center on Biology and Chemistry, Shanghai Institute of Organic Chemistry, Chinese Academy of Sciences, Shanghai 201210, China. ³State Key Laboratory of Urban Water Resource and Environment, School of Environment, Harbin Institute of Technology, Harbin 150090, China. ⁴HIT Center for Life Sciences, School of Life Science and Technology, Harbin Institute of Technology, Harbin 150080, China. ⁵These authors contributed equally: Yanan Zhao, Jiaojiao Hu, Shan-Shan Yang.

✉ e-mail: fanyang115@hit.edu.cn

designer AcrIIIC1 with an improved inhibition potency was successfully employed as a switch to modulate the activity of a hepatocyte-specific *SauCas9* through the Cas-ON approach^{15,16}. Therefore, a comprehensive understanding of the regulation mechanism of Acrs for binding and inhibiting Cas9 is essential for advancing our fundamental knowledge of CRISPR biology, and for exploiting naturally evolved inhibitors of CRISPR-Cas technology.

In this work, we find that, in addition to a well-characterized monomeric species, AcrIIIC1 from *Neisseria meningitidis* (*NmeAcrIIIC1*) can assemble into an inactive dimer under oxidizing conditions. The inactive dimer can reversibly convert into the active monomer under reducing conditions. A further mechanistic study demonstrated that *NmeAcrIIIC1* employs two conserved cysteines to form two pairs of intermolecular disulfide bonds to mediate the dimer's assembly. This enables a redox switch that also applies to two phylogenetically related AcrIIIC1 orthologs we tested, indicative of the redox switch's biological significance. More importantly, with the knowledge of the structural and chemical basis of the redox switch of wild-type *NmeAcrIIIC1*, we successfully generated an AcrIIIC1 mutant with its inactive oxidized state suppressed. This mutant AcrIIIC1 may serve as a stable and robust inhibitor of Cas9, resistant to redox fluctuation in various cellular environments, and is beneficial for CRISPR biotechnology.

Results

NmeAcrIIIC1 assembles into a homodimer triggered by oxidation

To investigate the structure and activity of *NmeAcrIIIC1*, we first purified the *NmeAcrIIIC1* protein overexpressed in *Escherichia coli* (*E. coli*). Under reducing conditions, the size-exclusion chromatography (SEC) profile shows a single peak at ~10 kDa corresponding to the monomeric species, consistent with the previous studies¹⁴. Surprisingly, we observed that, in

the absence of a reductant in the purification buffer, *NmeAcrIIIC1* proteins eluted as two separate peaks with apparent molecular weight at 9.6 and 19.3 kDa (Supplementary Fig. 1a, b) on an SEC column. In contrast, SDS-PAGE gel shows a single band at ~10 kDa for both peaks, the correct molecular weight for the *NmeAcrIIIC1* monomer (Supplementary Fig. 1c). Further, ¹H NMR spectra show that the two species are highly similar but not identical (Supplementary Fig. 1d), supporting dimer and monomer, respectively, with similar conformation.

Intriguingly, we noticed that the proportion of dimeric species dramatically increased when the protein sample was kept longer under oxidizing conditions before loading onto the SEC column. This behavior of *NmeAcrIIIC1* is highly reminiscent of proteins with redox states: the oxidized state gradually dominates over the time course of exposure to the air. To examine whether the interconversion between the dimer and monomer of *NmeAcrIIIC1* is under redox regulation, we added excess dithiothreitol (DTT) to the dimer eluent and excess hydrogen peroxide (H₂O₂) to the monomer eluent, respectively, and examined the change of their retention positions on the SEC column. In line with our hypothesis, the dimer converted into a monomer by reduction of excess DTT, and the monomer converted into a dimer by oxidation of H₂O₂ (Fig. 1a). We further performed native PAGE gel and Ellman's assay to assess the oxidized states of *NmeAcrIIIC1* induced in two ways, either by the air or by the oxidant such as H₂O₂. As shown in Supplementary Fig. 2a, the result of native PAGE shows a band with the same size at less than 25 kDa for the oxidized *NmeAcrIIIC1* induced in either way, in comparison with the reduced band at less than 15 kDa. In addition, Ellman's assay result demonstrates no residual -SH groups for the oxidized *NmeAcrIIIC1* induced in, either way, provided an accurate amount of -SH for the reduced *NmeAcrIIIC1* can be calculated against the standard curve fitted with gradient concentrations of DTT mixed with excess DTNB (Supplementary Fig. 2b). Collectively, the

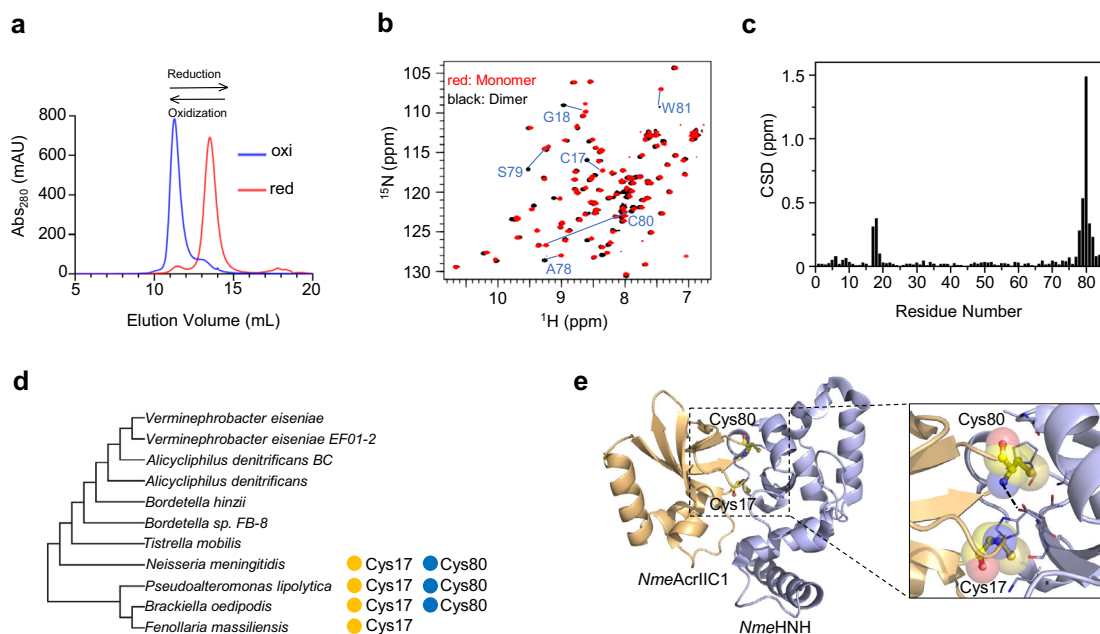


Fig. 1 | *NmeAcrIIIC1* can be oxidized into a dimer mediated by two conserved cysteines. **a** SEC runs show that the retention volume of *NmeAcrIIIC1* changes under different redox conditions. When oxidized, *NmeAcrIIIC1*'s apparent molecular weight becomes twice as the reduced one, corresponding to a dimer (Supplementary Fig. 1a). **b** Overlay of ¹H-¹⁵N HSQC spectra for the oxidized dimer and the reduced monomer of *NmeAcrIIIC1*. The peaks from the monomer and the dimer are colored red and black, respectively. Residues with significant chemical shift difference (CSD) between the two states are indicated by blue lines and labeled. **c** The bar diagram representing the composite CSDs ($\Delta\delta = [(\delta_{\text{HN}})^2 + (\delta_{\text{N}}/6.51)^2]^{1/2}$)

of the HN cross-peaks between the two redox states of *NmeAcrIIIC1*, as a function of the residue number. **d** Cys17 and Cys80 of *NmeAcrIIIC1* are present across three related orthologs in the unscaled phylogenetic tree. Cys17 is present in one more related species. A full sequence alignment can be found in Supplementary Fig. 1e. **e** The location of Cys17 and Cys80 of *NmeAcrIIIC1* in its complex with *NmeHNH* (PDB entry 5VGB) is focused with a dotted square. A close-up view of this region with the side chains of Cys17 and Cys80 highlighted with spheres is shown on the right. Source data are provided as a Source Data file.

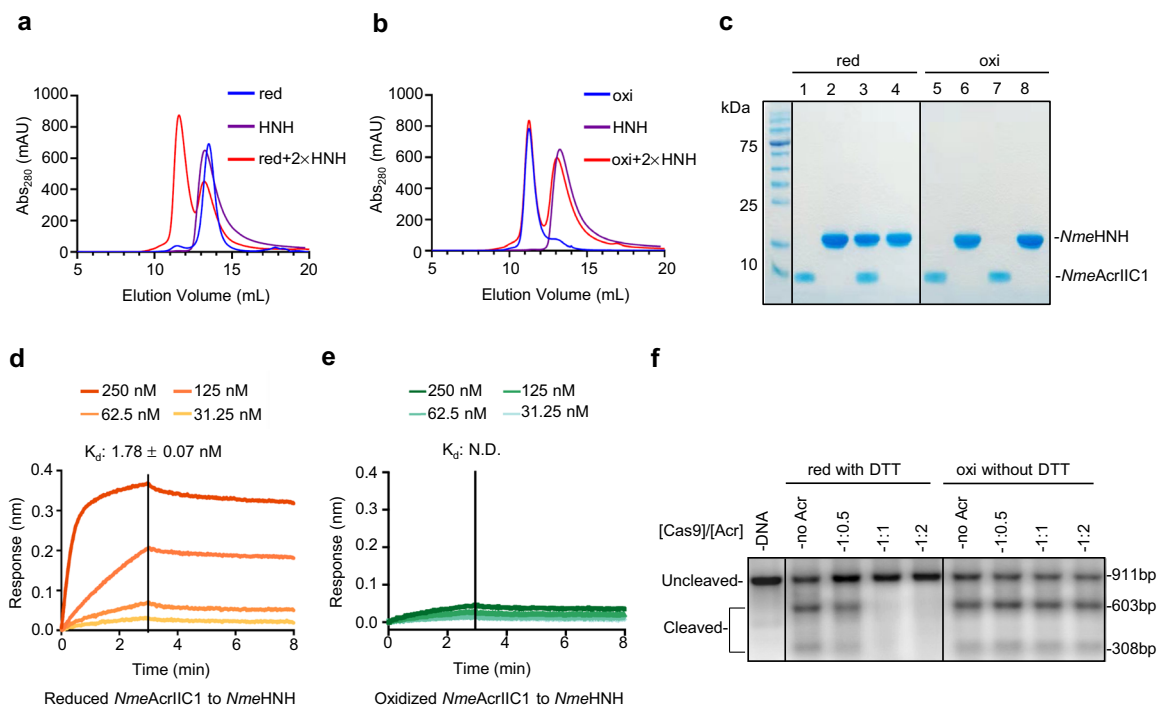


Fig. 2 | The oxidized *NmeAcrIIC1* loses its inhibitory activity against Cas9.

a Elution profiles of the SEC binding assay for the reduced *NmeAcrIIC1* (blue), *NmeHNH* (purple), or the two incubated together with twofold excess *NmeHNH* (red). The concentration for each trace was normalized to 0.1 mM of a single protein. **b** Elution profiles of the SEC binding assay for the oxidized *NmeAcrIIC1* (blue), *NmeHNH* (purple), or the two incubated together with twofold excess HNH (red). **c** Fractions from the assays shown in **a**, **b** were visualized on a 12% SDS-PAGE gel. Lane 1 to 4 corresponds to reduced *NmeAcrIIC1*, *NmeHNH*, the complex fraction from the mixture of reduced *NmeAcrIIC1* with twofold excess *NmeHNH*, and the residual *NmeHNH* from the mixture above. Lane 5 to 8 corresponds to oxidized

NmeAcrIIC1, *NmeHNH*, the earlier eluent from the mixture of oxidized *NmeAcrIIC1* with twofold excess *NmeHNH*, and the latter eluent from the mixture above.

d, **e** Binding affinities determined by BLI for the reduced *NmeAcrIIC1* and the oxidized *NmeAcrIIC1* to *NmeHNH*, respectively. The reduced *NmeAcrIIC1* shows a K_d of 1.78 nM, while the oxidized *NmeAcrIIC1* gives a very weak response <0.05 , indicating very poor binding. **f** DNA cleavage assays were conducted in the presence of the reduced *NmeAcrIIC1* with five-fold excess DTT (relative to Acr) in the buffer, and the oxidized *NmeAcrIIC1* without DTT, respectively. Data were replicated independently more than three times with similar results and the representative one is shown. Source data are provided as a Source Data file.

oxidized forms of *NmeAcrIIC1* induced in two ways are identical in terms of their oligomeric and redox states. To be consistent, for the following assays, we made the oxidized *NmeAcrIIC1* by using H_2O_2 , which takes a shorter incubation time as long as an appropriate amount of oxidant is used.

We next characterized the two redox forms of *NmeAcrIIC1* by using NMR spectrometry. We prepared the ^{15}N and ^{13}C labeled protein samples of monomer and dimer, collected 2D 1H - ^{15}N HSQCs, and assigned the backbone H-N cross-peaks using standard triple resonance procedures for each of them. As shown in Fig. 1b, the 1H - ^{15}N HSQC counts about 80 sharp and well-dispersed peaks with almost even intensities for the monomer. Strikingly, the 1H - ^{15}N HSQC spectrum for the dimer also shows a set of ~80 cross-peaks, indicative of a symmetric structure, at least when averaged over the NMR time scale. Moreover, the 1H - ^{15}N HSQC spectrum of the monomer spontaneously turned into that of the oxidized dimer induced with H_2O_2 , further confirming that the oxidized *NmeAcrIIC1* induced by different ways are identical from a structural perspective (Supplementary Fig. 2c).

Notably, the two HSQCs of *NmeAcrIIC1* monomer and dimer overlap quite well. Only less than ten residues sequentially adjacent to Cys17 and Cys80 exhibit significant large chemical shift deviation (CSD) (Fig. 1c), which strongly suggests that Cys17 and Cys80 could be the key residues triggering the redox state transition. Importantly, phylogenetic analysis of 11 *AcrIIC1* orthologs from different bacteria originally annotated by Pawluk et al.⁸ shows that Cys17 and Cys80 in *Nme* are conserved across at least three related species (Fig. 1d and Supplementary Fig. 1e), further supporting their functional roles from an evolutionary standpoint. In addition, by carefully examining the structure of *NmeAcrIIC1* bound to the HNH nuclease reported

previously¹⁴ (Fig. 1e), we noticed that Cys17 and Cys80 are both located on the protein surface. More importantly, both cysteines are involved in the interface of *NmeAcrIIC1*'s complex with HNH nuclease and play a role in the interaction. Since our study shows that Cys17 and Cys80 are also involved in dimer formation, we hypothesized that dimeric *NmeAcrIIC1* would be unable to bind Cas9.

The oxidized dimer of *NmeAcrIIC1* cannot bind to HNH and therefore loses its inhibitory activity against Cas9

Structural work demonstrated that *AcrIIC1* functions through binding to and conformationally restraining the HNH nuclease of Cas9¹⁴. We thus examined whether the oxidized dimer of *NmeAcrIIC1* can bind to HNH nuclease and exert inhibitory activity against Cas9 like its reduced monomeric form. We characterized the interaction between *NmeAcrIIC1* and *NmeHNH* with SEC and measured the equilibrium binding affinity by Bio-Layer Interferometry (BLI). We first incubated the reduced *NmeAcrIIC1* with twofold excess *NmeHNH* and fractionated the mixture over a Superdex 75 SEC column. A significant shift of *NmeAcrIIC1* was observed due to the binding of *NmeAcrIIC1* to *NmeHNH* (Fig. 2a, c). In sharp contrast, incubated with two fold excess *NmeHNH*, the oxidized *NmeAcrIIC1* showed no shift, indicative of no binding with *NmeHNH*, at least at μM concentration used for SEC (Fig. 2b, c). To further measure the detailed binding kinetics for both states of *NmeAcrIIC1* to *NmeHNH*, we performed BLI to obtain the equilibrium dissociation constant K_d . Fitting of the data yielded a K_d value of 1.8 nM for the reduced *NmeAcrIIC1* (Fig. 2d), comparable to 6.3 nM previously measured by Isothermal Titration Calorimetry (ITC)¹⁴. Yet, for the oxidized *NmeAcrIIC1*, we were unable to measure any appreciable affinity (Fig. 2e).

Additionally, we performed the NMR titration experiments to explore the interactions of different redox forms of *NmeAcrIIIC1* with *NmeHNNH* at an atomic level. Consistent with previous results, NMR titration of the reduced *NmeAcrIIIC1* with *NmeHNNH* yielded another set of cross-peaks being in slow conformational exchange with the original peaks, indicative of strong interaction between the titrate and the titrant with a K_d falling into nM- μ M range, shown in Supplementary Fig. 3a. In sharp comparison, the titration of the oxidized *NmeAcrIIIC1* with *NmeHNNH* didn't change the cross-peaks even at a half mM concentration (Supplementary Fig. 3b).

Given the loss of the interaction of the oxidized *NmeAcrIIIC1* to *NmeCas9*, we next sought to examine whether the oxidized *NmeAcrIIIC1* dimer exhibits inhibitory activity against *NmeCas9*. We conducted well-established DNA cleavage assays in the presence of an Acr protein in vitro. We set up the DNA cleavage assay with the reduced and the oxidized *NmeAcrIIIC1* under reducing and non-reducing conditions, respectively (Fig. 2f). Under the reducing condition, with DTT (five-fold excess relative to Acr) maintained in the reaction buffer, the reduced *NmeAcrIIIC1* was able to inhibit the DNA cleavage by *NmeCas9* completely with only a 1:1 ratio of Cas9 to Acr. In contrast, under the non-reducing condition containing no reductant in the reaction buffer, the oxidized *NmeAcrIIIC1* showed no impact on *NmeCas9*'s function at all, even at a higher Acr ratio of 1:2. This result demonstrates that the oxidized dimer of *NmeAcrIIIC1* represents its inactive state without Cas9 inhibitory activity.

Structures of the two redox states of *NmeAcrIIIC1*

To further delineate the structural basis underlying the formation of the inactive dimeric state of *NmeAcrIIIC1*, we set out to determine the structures of both redox states of *NmeAcrIIIC1*. We first performed solution NMR to determine the structure of the monomeric reduced *NmeAcrIIIC1*. With larger than 90% of the chemical shifts for the backbone and the side chains assigned, combined with a good number of NOE-derived distance restraints (Supplementary Table 1), we obtained a high-quality ensemble of solution structure for the reduced *NmeAcrIIIC1*. The superposition of the 20 lowest-energy conformers together with the ribbon diagram of the representative structure is shown in Fig. 3a, b. The root mean square deviation (RMSD) of the 20 conformers for the backbone of the secondary structural region is only 0.19 Å, indicating an ordered and rigid conformation. Overall, the reduced *NmeAcrIIIC1* adopts a similar conformation with a $\beta 1\beta 2\beta 3\alpha 1\alpha 2\beta 4\beta 5$ topology as its holo-form in complex with *NmeHNNH*, exhibiting an RMSD of 1.00 Å for the full-length backbone (Supplementary Fig. 4a). Importantly, Cys17 and Cys80 are highly solvent-exposed in the monomeric structure, and their side chains exhibit multiple conformations on NMR time scale (Fig. 3a), in support of our hypothesis that these two cysteines could be redox-active.

For the oxidized dimer, NMR experiments showed that the chemical shifts for C_β of Cys17 and Cys80 shift downfield to 44.3 and 37.1 ppm, respectively, revealing that Cys17 and Cys80 are both involved in the disulfide linkage¹⁷ (Supplementary Fig. 4b). However, our efforts to obtain intermolecular restraints using ^{15}N , ^{13}C -filtered/ ^{15}N , ^{13}C -edited NOESY experiments were unsuccessful. Fortunately, we managed to grow protein crystals formed by the oxidized *NmeAcrIIIC1* and solve the crystal structure of the dimer with a resolution of 1.61 Å by using X-ray crystallography (Supplementary Table 2). As shown in Fig. 3c, in the dimeric structure, one of the protomers is rotated roughly 180 degrees relative to the other partner, which then allows for the dimerization via two intermolecular disulfide bonds. Each subunit of the dimeric form aligns with the reduced monomeric form of *NmeAcrIIIC1* with a small RMSD of 0.68 and 0.73 Å, respectively (Supplementary Fig. 4c, d). Strikingly, the two subunits assemble mainly through two parallel intermolecular disulfide bonds formed by Cys17 and Cys80, but not hydrophobic or electrostatic interaction that is commonly observed in mediating protein-protein interaction. The subunit orientation of the

dimer is restricted to a great extent by the two intermolecular disulfide bonds, shown in Fig. 3c, d. This unique dimerization pattern is critical in regulating the dynamic switches between the active monomer and the inactive dimer in response to different redox conditions, which will be discussed in the next section of the results.

To preclude an artificial structural arrangement caused by crystal packing, we further investigated the behavior of the dimer in solution by NMR. First, in this scenario where redox state exchange is coupled with monomer-dimer conversion, CSD uncovers residues impacted either by thiol-disulfide bond transition or by interfacial contacts to the other subunit. We observed that significant CSDs only occur for the residues next to Cys17 and Cys80 but not to other regions (Fig. 1b, c), which echoes the crystal structure that Cys17 and Cys80 are the key residues involved in the dimer interface. Second, the estimated rotational correlation time (T_c) for the oxidized dimer is almost twice as that for the reduced monomer (11.6 versus 6.0 ns), whereas the trends of ^{15}N backbone relaxation data of R_1 , R_2 , and Het-NOE align well between the two states on a residue-by-residue base, which reveals a rigid dimer with restricted orientation for each subunit but lacking large interfacial surface that is supposed to alter the dynamic properties of the residues involved (Fig. 3e). Together, the CSD and ^{15}N relaxation data for both forms of *NmeAcrIIIC1* in solution strongly support the crystal structure, stating that the crystal structure of the oxidized dimer can reliably represent the dimer's behavior in solution.

Importantly, compared with the structure of *NmeAcrIIIC1*'s complex with *NmeHNNH*, the counterpart subunit of dimeric *NmeAcrIIIC1* occupies the position of the *NmeHNNH*, burying the "hot spot" residue Ser79, thereby inhibiting the interaction between *NmeAcrIIIC1* with *NmeHNNH* through steric hindrance (Fig. 3f, g). Thus, the dimeric structure rationalizes how oxidization and dimerization of *NmeAcrIIIC1* result in the disruption of *NmeHNNH* binding and the loss of inhibitory activity against Cas9.

Cys17 and Cys80 form the key redox switch to mediate *NmeAcrIIIC1*'s redox cycle

We next asked whether *NmeAcrIIIC1* can be redox recycled both structurally and functionally via the pair of cysteines as a redox switch. First, we examined the interconversion of the redox structures by using ^1H - ^{15}N HSQC. Treated with excess H_2O_2 as the oxidant, the structure of the reduced *NmeAcrIIIC1* spontaneously turned into that of the oxidized/dimeric one. We were able to observe the conversion back to the monomeric form upon the addition of excess DTT to overcome the oxidizing effects of H_2O_2 . This structural interconversion is marked by HN cross-peak shifts of the residues next to Cys17 and Cys80 (Fig. 4a, b). We next explored whether the functional activity of *NmeAcrIIIC1* is coupled with its structure and can be recycled in response to different redox conditions. NMR titration experiments showed H_2O_2 -processed *NmeAcrIIIC1* loses its binding to *NmeHNNH*, while the re-reduced *NmeAcrIIIC1* from the H_2O_2 -processed one can bind to *NmeHNNH* as competent as the nascent one. Furthermore, we performed the DNA cleavage assay to assess the inhibitory activity of *NmeAcrIIIC1* within the redox cycle. The inhibitory activity of the reduced *NmeAcrIIIC1* was completely impaired by the addition of excess H_2O_2 , and then 100% recovered after the addition of excess DTT (Fig. 4c, d). Thus, our results show that the structure and functional activity of *NmeAcrIIIC1* can be recycled between its different redox states.

At the molecular level, good redox switches should be accessible and have intermediate half-lives and sufficient reactivity¹⁸. According to these criteria, the pair of Cys17 and Cys80 qualifies as a superior redox switch supported by three lines of evidence: First, as shown in the structures of both redox states of *NmeAcrIIIC1* (Fig. 3a–d), Cys17 and Cys80 are indeed highly accessible in forms of either thiols or disulfide bonds. Second, by examining the electron density map of the oxidized *NmeAcrIIIC1*, we observed that both of the intermolecular

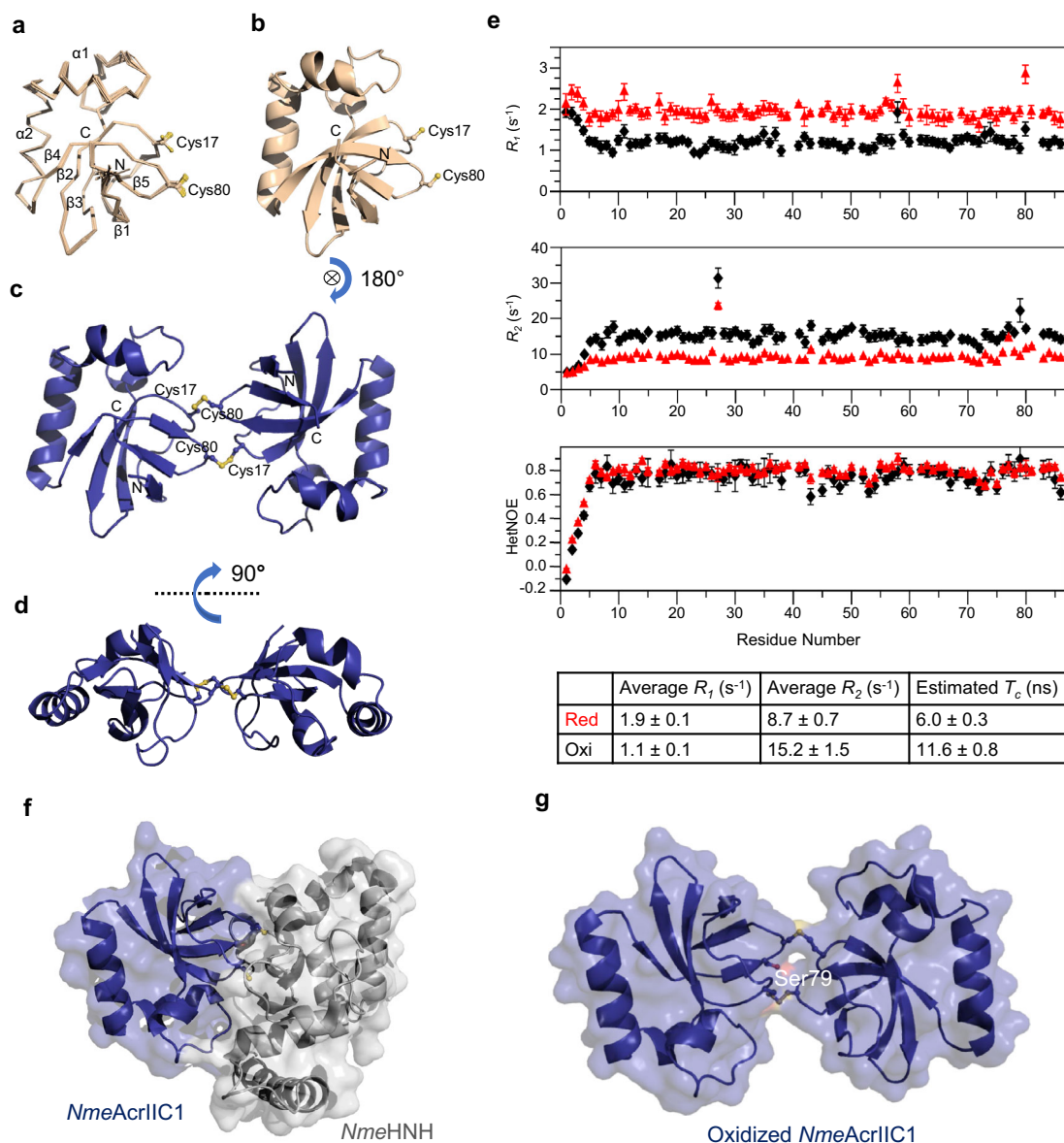


Fig. 3 | Structures and dynamics for both redox states of *NmeAcrIIc1*.

a Superposition of the 20 lowest-energy structures of the reduced *NmeAcrIIc1* calculated using solution NMR. Secondary structures are labeled, and the side chains of Cys17 and Cys80 are drawn in sticks. **b** The representative lowest-energy structure of the reduced *NmeAcrIIc1* is shown in the ribbon diagram. **c** Crystal structure of the dimeric oxidized *NmeAcrIIc1*. **d** The same as **c**, rotated by 90° along the horizontal axis drawn in a dotted line. **e** ¹⁵N backbone relaxation data for the reduced *NmeAcrIIc1* (red) and the oxidized *NmeAcrIIc1* (black). ¹⁵N longitudinal relaxation rate constant R_1 (top panel), ¹⁵N transverse relaxation rate constant R_2

(middle panel), and heteronuclear ¹H-¹⁵N NOE values (bottom panel) plotted as a function of the residue number. Rotational correlation times T_c were estimated using average R_1 and R_2 using Eq. (1) and listed in the table below. $n = 2$ independent experiments have been performed. Dots represent mean and error bars represent SD. **f** Surface representation of the complex structure of *NmeAcrIIc1* bound to *NmeHNH*. **g** Surface representation of the structure for the oxidized *NmeAcrIIc1*. Residue Ser79, crucial to the recognition of *NmeHNH*, is highlighted and labeled. Source data are provided as a Source Data file.

disulfide bonds are not fully occupied, indicative of dynamic short-lived chemical groups (Supplementary Fig. 5a). Third, the pK_a values of Cys17 and Cys80 determined using pH titration are 8.9 and 8.3, respectively (Supplementary Fig. 5b), shifting from the average value (8.5 ± 0.5) in the opposite direction¹⁹. This significant pK_a shifting indicates strong interactions could occur between Cys17 and Cys80 by sharing the proton remaining on the Cys17 after the ionization of Cys80, consequently accelerating the redox reaction^{20,21}. Taken together, our results demonstrate that the Cys17-Cys80 pair serves as a highly active redox switch to mediate the redox cycle of *NmeAcrIIc1* for dynamically regulating its functional activity in response to different redox conditions.

AcrIIc1 variant with robust anti-Cas9 activity in diverse redox environments

As the oxidative condition can diminish the activity of *NmeAcrIIc1*, we next asked whether we could generate a robust *NmeAcrIIc1* with potent and constant activity irrespective to various redox environments. Based on our structural and functional studies, we optimized *NmeAcrIIc1* with Cys17 and Cys80 replaced to suppress the formation of its inactive oxidative state. In one mutant, the two cysteines are substituted with serine residues due to structural similarity, designated as AcrIIc1-SS. The other mutant uses alanine instead of serine (AcrIIc1-AA) to explore whether a smaller side chain could benefit when interacting with *NmeHNH*. Initial in silico evaluation of their

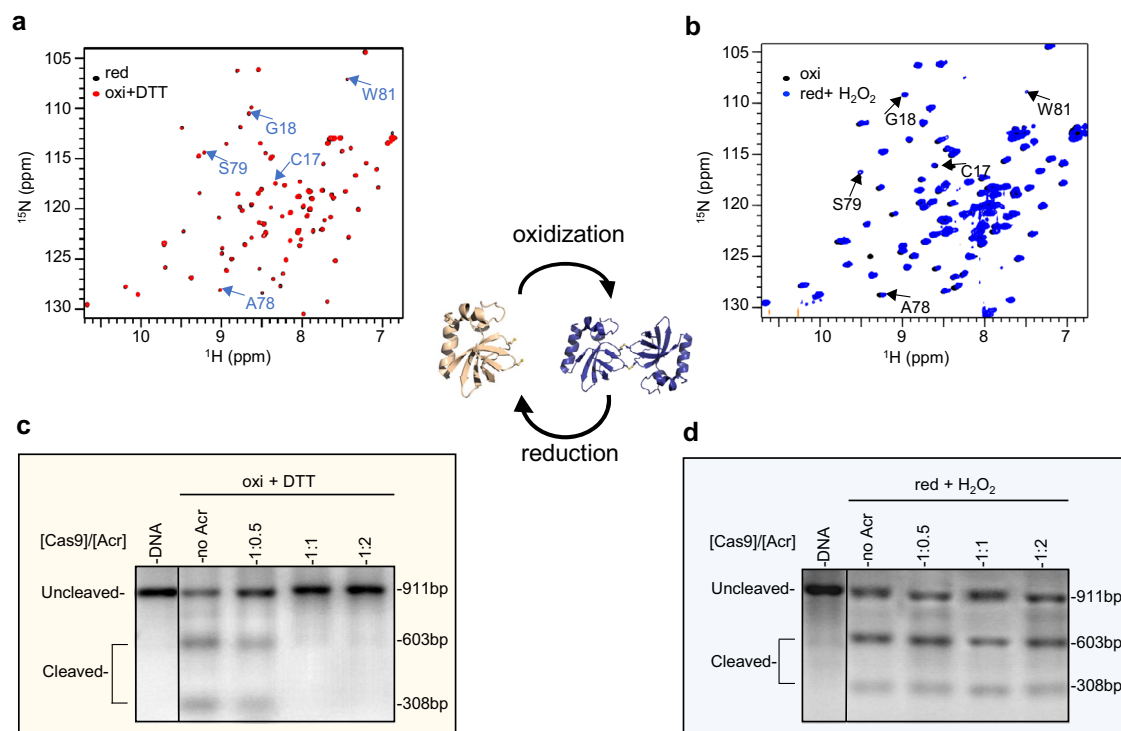


Fig. 4 | The two redox states of *NmeAcrIIC1* can be interconverted and mediated by the pair of Cys17-Cys80. **a** Superimposition of ^1H - ^{15}N HSQC spectra of the reduced *NmeAcrIIC1* (black) and that after recycling from the oxidized state (red). To better demonstrate the change of the structure from ^1H - ^{15}N HSQC, peaks with significant CSD between the two states of *NmeAcrIIC1* are indicated with blue arrows and labeled. **b** Superimposition of ^1H - ^{15}N HSQCs of the oxidized *NmeAcrIIC1*

(black) and that after recycling from the reduced state (blue). **c** The DNA cleavage reaction inhibited by the re-reduced *NmeAcrIIC1* from its oxidized state. **d** The result of DNA cleavage assay in the presence of an increasing ratio of the H_2O_2 -oxidized *NmeAcrIIC1*. The DNA cleavage assays have been repeated independently more than three times with similar results. Source data are provided as a Source Data file.

interfacial contacts to *NmeHNNH* using Rosetta InterfaceAnalyzer²² suggested that, the side chain -OH from serine of AcrIIC1-SS would better mimic the -SH from cysteine of the wild-type *NmeAcrIIC1* and near-completely reserves the hydrogen bonding to *NmeHNNH* (Fig. 5a). In addition, the Rosetta outputs favor the AcrIIC1-SS mutant in several aspects, including better shape complementary value, larger interface surface area, etc. Thus, we chose AcrIIC1-SS for the following functional experimental assessment.

To examine the functional behavior of AcrIIC1-SS, we measured AcrIIC1-SS's binding capacity to *NmeHNNH* using BLI and NMR titration, and its inhibitory activity against Cas9 using DNA cleavage assay. With or without reductants in the buffer, AcrIIC1-SS exhibits a K_d to *NmeHNNH* at 12.7 or 10.8 nM (Fig. 5b and Supplementary Fig. 6a), achieving comparable binding affinity as that of the wild-type AcrIIC1 (wtAcrIIC1). Consistent with this strong interaction, NMR titration and gel filtration result of AcrIIC1-SS with *NmeHNNH* revealed a tight binding with a similar slow-exchange pattern as the wtAcrIIC1 (Supplementary Fig. 6b–d). Most importantly, with the redox-sensitive cysteines being replaced, AcrIIC1-SS doesn't undergo the redox cycle as wtAcrIIC1 does, offering better stability over wtAcrIIC1 under various redox conditions (Fig. 5c). As for the activity, under reducing conditions, AcrIIC1-SS inhibits the DNA cleavage activity of Cas9 to a comparable extent as the wtAcrIIC1 (Fig. 5d top panel). Moreover, in sharp contrast to the significant drop of the inhibitory activity of wtAcrIIC1, the activity of AcrIIC1-SS remains constantly high under various non-reducing conditions, either exposed to the atmosphere or excess H_2O_2 (Fig. 5d middle and lower panel). Thus, as summarized in Fig. 5e, wtAcrIIC1's activity is prone to vary upon redox potential changes and can undergo inactivation via disulfide-mediated dimerization. Whereas, with the redox-sensitive Cys residues being replaced without compromising its binding capability to Cas9, AcrIIC1-SS would not be

affected by redox potential fluctuation, serving as a highly robust AcrIIC1 variant.

To further investigate the redox regulation of wtAcrIIC1 biologically and to examine how robust AcrIIC1-SS behaves in various redox environments in cells, we established an antimicrobial susceptibility assay to qualitatively assess the anti-CRISPR activity of AcrIIC1 in *E. coli*. Taking advantage of the pCas-pSG-mediated constitutive expression of Cas9 and a sgRNA targeting the kanamycin resistance gene²³, we succeeded to observe a larger inhibition ring around the paper disk impregnated with kanamycin on the bacterial lawn of growth relative to the negative control, as shown in Fig. 6a–c panel 1, 2. Very importantly, co-expression of wtAcrIIC1 induced by IPTG restored the inhibition zone to a comparable size where no CRISPR-Cas9 functions (Fig. 6a, c panel 3, 4), strongly indicating that Cas9 is mostly inhibited by the overexpressed wtAcrIIC1. By contrast, the inhibition zone expanded to a similar size as where wtAcrIIC1 was not expressed, when the bacterial cells were exposed to 1 mM H_2O_2 during wtAcrIIC1 expression, implying substantial activity loss of wtAcrIIC1 under the oxidative environment (Fig. 6a, c panel 5, 6). Moreover, native PAGE gel confirmed almost complete conversion of wtAcrIIC1 to its oxidized dimeric form in the cell under H_2O_2 stimulus (Supplementary Fig. 7a). Not surprisingly, when co-expressed with AcrIIC1-SS, the inhibition zone remained the same size with or without H_2O_2 stimulus, as shown in Fig. 6b, c panel 3, 4, 5, 6, stating that AcrIIC1-SS behaves as a superior Cas9 inhibitor with more stable activity in vivo.

Discussion

Bacterial cells are constantly experiencing redox potential fluctuation, caused by reactive oxygen species (ROS) generated as a product of aerobic metabolism or exogenous stimuli such as UV radiation and oxidative stress from host defense. To adapt to this redox variation,

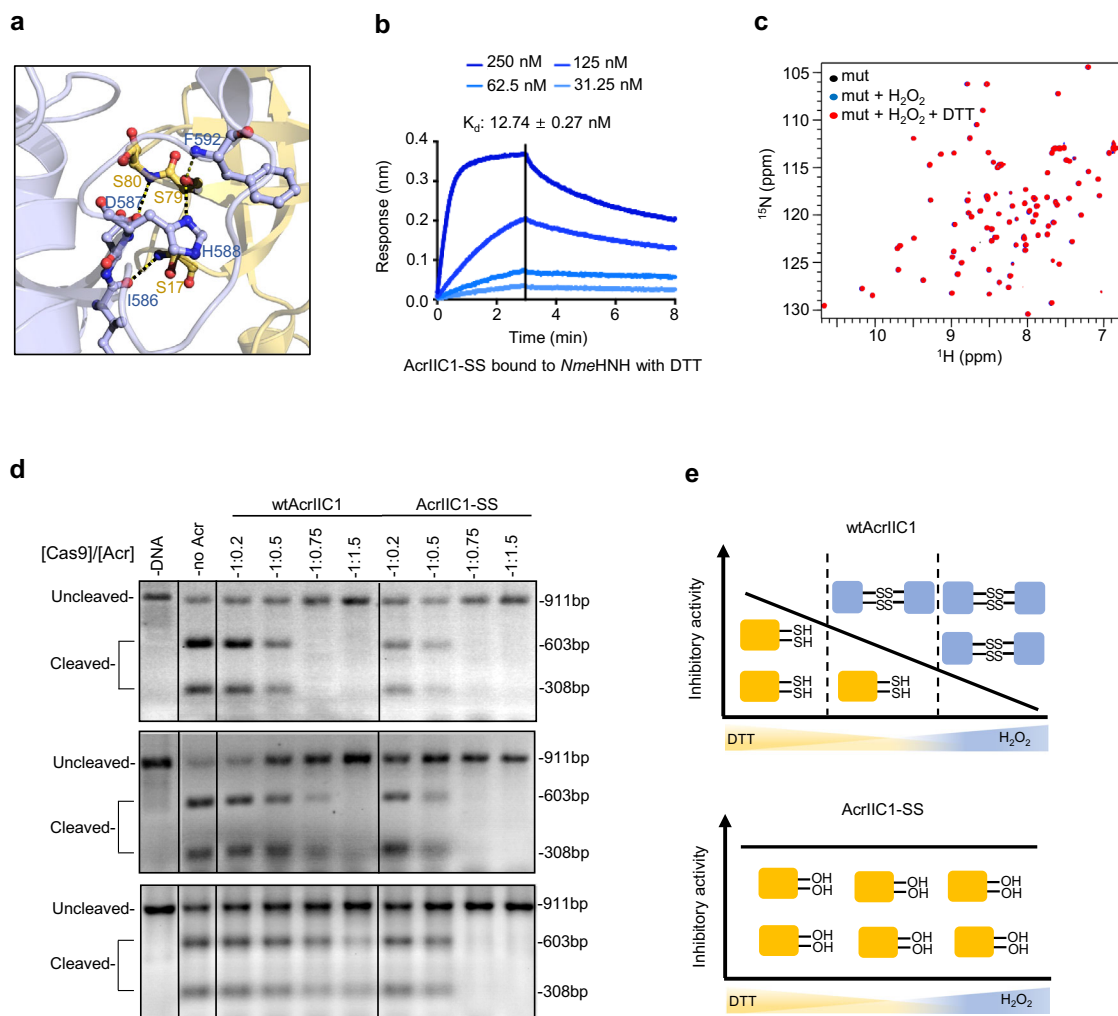


Fig. 5 | AcrIIIC1-SS is a robust AcrIIIC1 variant. **a** A close-up view of the interface of AcrIIIC1-SS in complex with NmeHNH. The structural model was built using the SWISS-MODEL website (<https://swissmodel.expasy.org>) with PDB entry 5VGB as the template. AcrIIIC1-SS is colored yellow and NmeHNH is colored purple. Key residues involved in interfacial hydrogen bonds are drawn in sticks and labeled. **b** K_d determined by BLI for AcrIIIC1-SS bound to NmeHNH is 12.7 nM with excess DTT in the reaction buffer. **c** Overlay of ^1H - ^{15}N HSQC spectra of AcrIIIC1-SS (black), AcrIIIC1-SS treated with excess H_2O_2 (blue), and AcrIIIC1-SS treated with H_2O_2 and more DTT in sequence (red) indicate the structure of AcrIIIC1-SS is not affected by redox

reagents. **d** DNA Cleavage assays were conducted with wtAcrIIIC1 and AcrIIIC1-SS under different redox conditions. Three reaction conditions were used: the reducing condition with 1 mM DTT in the buffer (top panel), the non-reducing condition without DTT or H_2O_2 in the buffer (middle panel), and the oxidizing condition with a fivefold molar ratio of H_2O_2 relative to Acr in the buffer (bottom panel). The experiments have been repeated more than three times with similar results. **e** Schematic representation of the inhibitory activities of wtAcrIIIC1 (top) versus AcrIIIC1-SS (bottom) under different redox environments. Source data are provided as a Source Data file.

bacteria have evolved a comprehensive redox signaling system involving a large number of redox-sensing regulatory proteins²⁴. Our study reveals a naturally occurring redox switch of NmeAcrIIIC1. Moreover, we demonstrate that NmeAcrIIIC1 is subject to dynamic redox regulation both structurally and functionally mediated by a key cysteine pair, which is conserved in the other two AcrIIIC1 orthologs from phylogenetically related species *Brackiella oedipodis* (Boe) and *Pseudomonas lipolytica* (Pli). Importantly, by using SEC and NMR ^1H spectra, we demonstrated that these two AcrIIIC1 orthologs undergo redox cycles as well. As for BoeAcrIIIC1, which shares 28.4% of sequence identity with NmeAcrIIIC1, we observed a similar pattern of monomer-dimer structural transition in response to redox condition change in the buffer (Supplementary Fig. 8a–c). PliAcrIIIC1, which contains an extra alpha helix extended at its C-terminus as modeled by AlphaFold²⁵ (Supplementary Fig. 8d), is highly prone to aggregation under oxidizing conditions. Nevertheless, we observed the transition between the reduced monomer and the oxidized oligomers of PliAcrIIIC1 by using SEC and ^1H NMR spectra (Supplementary Fig. 8e–g). It's very possible that the redox switch identified from AcrIIIC1 may serve as a

common regulation mechanism shared by other Acr proteins. It's been only less than ten years since the first anti-CRISPR protein was identified²⁶, and there is so much to be uncovered in this field, including more members in the AcrIIIC1 family and other Acr proteins that might possess redox-sensitive cysteines.

Our in vitro assays demonstrated the redox switch of NmeAcrIIIC1 and elucidated the structural basis underlying this dynamic regulation process. Recent publications involving experimental studies for AcrIIIC1 indicate that previous in vitro assays were performed with reductants maintaining reducing experimental conditions (listed as Supplementary Table 3)^{8,12,14,15,27–31}. For example, in the structural study of NmeAcrIIIC1 complexed with HNH, they kept 0.5–1 mM TCEP-NaOH in all purification buffers and 1 mM DTT or 1 mM TCEP-NaOH for all in vitro cleavage and binding assays. It could be the reducing experimental condition that precluded the chance of forming the oxidized AcrIIIC1. As for previous in vivo assays, since only apparent activity of AcrIIIC1 can be observed without characterization of the molecular state, it's hard to tell the exact redox state of AcrIIIC1 molecules in the cell. To assess the intracellular state

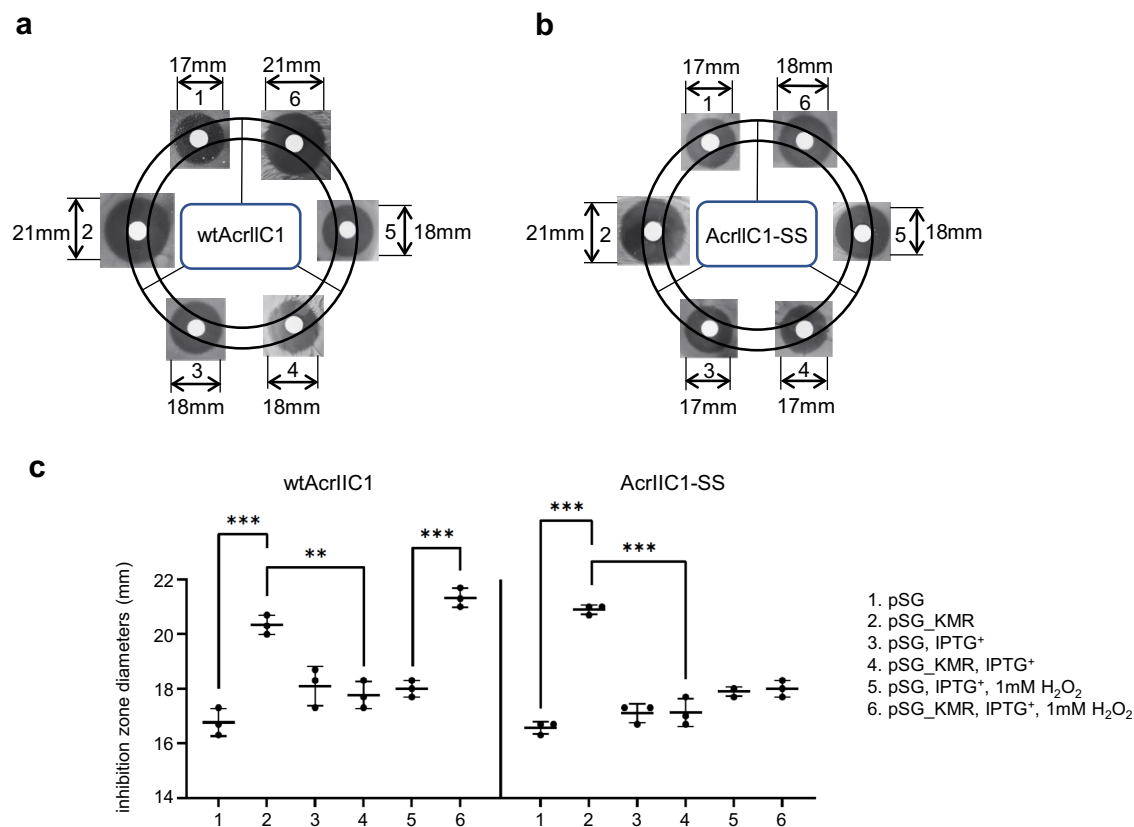


Fig. 6 | Antimicrobial susceptibility assays accessing wtAcrIIIC1 and AcrIIIC1-SS activities in vivo. **a** Panels 1, 2, assays without wtAcrIIIC1 expression: pSG represents negative control carrying no spacer; pSG_KMR represents *kmR* spacer-introduced plasmid. The gene-editing ability of the two-plasmid system pCas-pSG was confirmed by a significant increase in the size of the inhibition ring relative to the negative control, with a representative diameter of 21 mm vs 17 mm. Panels 3, 4, assays with wtAcrIIIC1 induced by IPTG. Co-expression of wtAcrIIIC1 restored the inhibition ring because it binds to and deactivates Cas9. Panels 5, 6, assays with wtAcrIIIC1 induced and 1 mM H₂O₂ stimulus. wtAcrIIIC1 failed to restore the inhibition ring under H₂O₂ stimulus due to the loss of its activity under the oxidative environment. **b** Co-expression of AcrIIIC1-SS can restore the inhibition ring under various redox environments because its activity is resistant to redox fluctuation.

Assay panels are in the same order as **a**. **c** Statistical analysis of the inhibition zone diameters from **a**, **b**. The left part shows the size of the inhibition ring varies in response to environmental redox change when wtAcrIIIC1 is co-expressed with Cas9. The right panel shows the size of the inhibition ring remains constant and resistant to environmental redox changes when AcrIIIC1-SS is co-expressed with Cas9. Lines in the plots indicate means, dots indicate individual data points from three independent experiments, and every dot is calculated by averaging three rings' diameters from one plate. Error bars represent SD. Unpaired two-sided *t*-test, ***P* < 0.01, ****P* < 0.001. The exact *P* values for wtAcrIIIC1 panels 1 with 2, 2 with 4, and 5 with 6 are 0.0005, 0.0019, and 0.0002, respectively. The *P* values for AcrIIIC1-SS panels 1 with 2 is <0.0001, and panels 2 with 4 is 0.0003. Source data are provided as a Source Data file.

of AcrIIIC1, we measured the redox potentials for the reducing buffers we used (listed as Supplementary Table 4), and compared them with the intracellular redox potentials reported previously. It seems that normal cytoplasmic values (−260 to −200 mV) fall within the range of our reducing buffers (−360 to −200 mV)^{32,33}, indicating most of the AcrIIIC1 molecules should be at their reduced state under normal physiological conditions. Under oxidative stress, local redox potential elevation in cells is not easy to measure at this point, due to the lack of a stable redox sensor working in this condition. However, it was reported that cells exposed to a more oxidizing potential (0 mV) had stimulated H₂O₂ production³⁴, which can induce the inactive dimer of AcrIIIC1 based on our in vitro and in vivo data. An important question is why do phages add this additional layer of regulation on AcrIIIC1? We propose one possible explanation: This inactivation mechanism evolved for AcrIIIC1, a broad-spectrum Cas9 inhibitor, could be an effective strategy for phage to fine-tune the level of active Acrs when its host bacterium experiences oxidative stress. Therefore, the phage could protect itself by helping its host to defend against other more lethal phages through CRISPR-Cas systems during stress, achieving a win-win situation with the host. Indeed, it was previously documented that prophages do help bacteria cope with adverse environments, including osmotic, oxidative, and acid stresses³⁵. Our work opens a door for investigating the

dynamic regulation of Acrs under the redox switch and leaves more critical questions to be addressed in the future.

As a key member of the Acr toolbox for Cas9-based gene editing, *NmeAcrIIIC1* has a wide range of applications in different cell types and tissues^{8,15}. From a biotechnological point of view, we should consider redox inactivation when applying *NmeAcrIIIC1*, potentially more other Acrs, in cells with unpredictable redox potential, such as cancer cells often with elevated levels of ROS³⁶. Recently, David Liu and co-workers discovered a bacterial toxin that can base-edit mitochondrial DNA³⁷. As for developing CRISPR-Cas systems for gene editing in mitochondria, excessive ROS as by-products of normal metabolism could be produced. Therefore, Acrs designed to function in a potentially oxidizing cellular environment should certainly avoid the redox effect in order to maximize their inhibitory activities. Herein, to perfect Acrs' behavior under various redox environments, we managed to generate a highly robust version of *NmeAcrIIIC1* with its redox-sensitive Cys residues replaced. The AcrIIIC1 variant has a comparable binding capability to the HNH nuclease of Cas9 as wtAcrIIIC1. Moreover, the inhibitory activity of the AcrIIIC1 variant is much higher than wtAcrIIIC1 under non-reducing environments, well suited to applications in cellular compartments with abnormally high ROS levels.

Additionally, we could take advantage of the redox regulation of Acrs to carry out tighter on-off control than direct regulation of the Cas

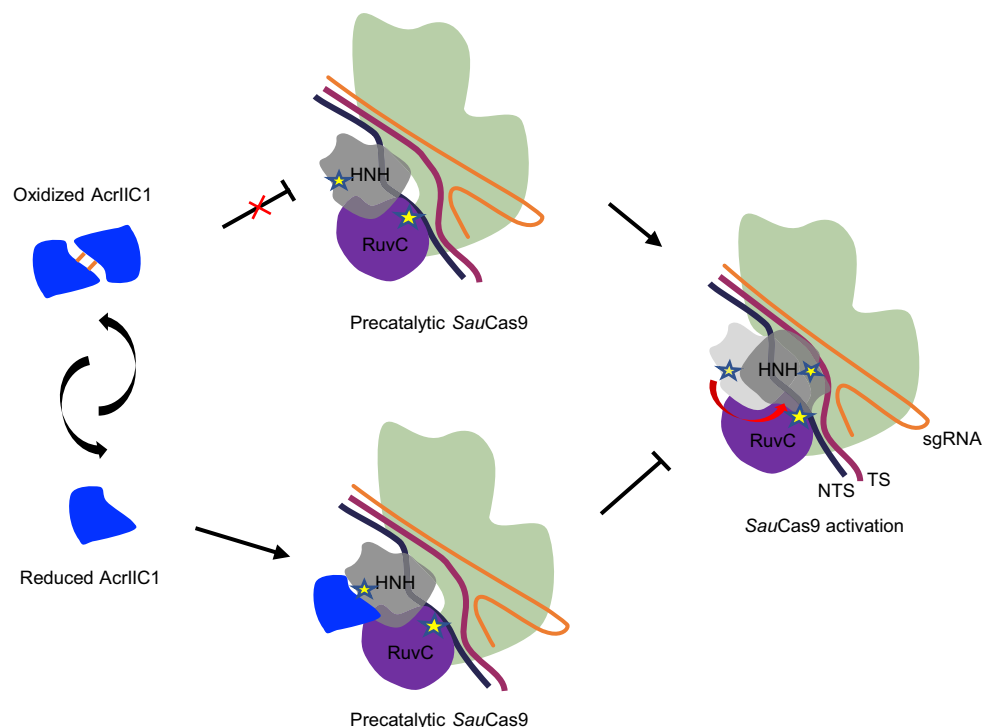


Fig. 7 | Schematic model demonstrating how different redox states of AcrIIIC1 affects the dynamics of Cas9 subunits and Cas9's activity. Reduced AcrIIIC1 would restrain the Cas9 complex at a precatalytic conformation through its

interaction with the HNH domain and deactivate Cas9, while oxidized AcrIIIC1 dimer would bury the contact interface with HNH, therefore loses its anti-Cas9 activity.

enzyme. Regulating Acrs to achieve more rapid and dynamic control of CRISPR-Cas activity has shown its feasibility⁶. Several methods for regulating Acr expression and activation have been developed, including transcriptional, post-transcriptional, optogenetic, and ligand-based strategies^{16,38–40}. Based on our findings, we might offer another option for fine-tuning the CRISPR-Cas system by indirectly regulating the redox potential, which could potentially achieve an elaborated control of Cas9's cleavage activity. Utilizing the *SauCas9* complex structure with its HNH domain bound to AcrIIA14⁴¹, we propose a schematic model demonstrating how different redox states of AcrIIIC1 would affect the dynamics of the Cas9 subunits and regulate Cas9's activity (Fig. 7). When sensing the environmental redox potential elevation, AcrIIIC1 molecule can dimerize with its closest partner and then loses its contact interface with HNH, so HNH may complete its conformational rearrangement positioning its catalytic site onto the DNA substrate. In contrast, in the reduced cellular environment, the monomeric AcrIIIC1 can bind to HNH and restrain the Cas9 complex at a precatalytic conformation without activity. Overall, our discovery of the naturally occurring redox switch for anti-CRISPR protein expands the regulatory toolset of the CRISPR system, and paves the road for further direction of engineering Acrs.

Methods

Protein expression and purification

The genes for *NmeAcrIIIC1*, *BoeAcrIIIC1*, *PliAcrIIIC1*, and *NmeHNH* were synthesized and sub-cloned into a modified pET-28a vector with a Protein G B1 domain (GB1) fused to the N-terminus, using cloning kit based on homologous recombination technology (Vazyme). The recombinant plasmids were transformed into *E. coli* BL21 (DE3) cells. Uniformed ¹⁵N- and ¹⁵N-, ¹³C- labeled proteins for NMR were obtained by growing the transformed cells at 25 °C in M9 minimal medium containing 0.5 g/L ¹⁵NH₄Cl, 2 g/L ¹³C-glucose supplemented with trace elements. Protein expression was induced with 0.5 mM IPTG when OD₆₀₀ of cells reached 0.6. After overnight, cells were harvested by

centrifugation and resuspended in lysis buffer (20 mM Tris, 500 mM NaCl, 10 mM imidazole, pH 8.0). The cell lysate was extracted by sonication and cleared by centrifugation. The supernatant was applied onto a HisTrap column (GE Healthcare) equilibrated in lysis buffer and the desired protein was eluted at ~250 mM imidazole. The pooled protein was incubated with in-house purified Tobacco Etch Virus (TEV) protease overnight and loaded onto HisTrap again to remove the cleaved His-GB1 tag and dialyzed into NMR buffer (20 mM Tris, 100 mM NaCl, pH 7.4). Protein samples were further loaded onto a Superdex 75 Hiload 26/60 (GE Healthcare) equilibrated with NMR buffer. The reduced AcrIIIC1s were supplemented with 1 mM DTT to maintain the reducing conditions. Purified proteins were then concentrated and stored at -80 °C for future use.

NMR spectroscopy

NMR spectra were collected at 25 °C on Bruker Avance 600 MHz spectrometer equipped with HCN cryogenic probes and pulse-field gradients. NMR data were processed with NMRPipe⁴² and analyzed with CCPNMR⁴³. 1D ¹H spectra were collected to compare the difference between the monomer and dimer of AcrIIIC1 orthologs. 2D ¹H-¹⁵N/¹³C HSQCs and 3D HNCO, HNCACB, CBCA(CO)NH, HBHA(CO)NH, HCCH-TOCSY, and (H)CCH-TOCSY were performed to obtain the chemical shift assignments of backbone and side chain atoms⁴⁴. 3D ¹³C-edited aliphatic and aromatic NOESY-HSQC (mixing time 100 ms) and ¹⁵N-edited NOESY-HSQC experiments (mixing time 100 ms) were collected to generate distance restraints for structural calculations.

Phylogenetic analysis

The accession numbers of AcrIIIC1 orthologs were acquired from a previous publication⁸, and the protein sequence for each AcrIIIC1 was downloaded from NCBI (<https://www.ncbi.nlm.nih.gov/protein/>). Proteins were aligned using ClustalOmega (<https://www.ebi.ac.uk/Tools/msa/clustalo/>) and an unscaled phylogenetic tree was built using MEGA software⁴⁵.

Size-exclusion binding assays

About 100 μM *NmeAcrIIC1* and 200 μM *NmeHNNH* were combined to a volume of 400 μL , incubated for 10 min, and injected onto a Superdex 75 Increase 10/300 GL (Cytiva) with a 500 μL sample loop at 0.5 mL/min flow rate using an AKTA Purifier 10 FPLC system (GE Healthcare). The binding buffer is the same for NMR measurements, with 1 mM DTT supplemented only for the reduced *NmeAcrIIC1*. Fractions were analyzed on a 12% SDS-PAGE gel and stained with Coomassie blue.

Ellman's assays

Ellman's reagent, DTNB (5,5'-dithio-bis-(2-nitrobenzoic acid)) (Bio-topped Life Sciences), was used to measure the free sulfhydryl groups in the protein solution. DTNB was dissolved to 100 mM in a reaction buffer of 20 mM Tris, pH 7.4, and 100 mM NaCl as a stock solution. To prepare the standards, DTT was dissolved in the reaction buffer with a gradually increased concentration (10, 20, 30, 40, and 50 μM). A final concentration of 10 mM DTNB was added and mixed with the standards. Absorbance at 412 nm (1 cm light path) was read by NanoDrop 2000C (Thermo Scientific) after 15 min of incubation. Each group was measured in double. Experiments were performed in triplicate. GraphPad Prism 8 was used to plot the absorbance values obtained for each standard against DTT concentrations, as shown in Supplementary Fig. 2b. The free sulfhydryl groups of the protein sample (concentration of ≤ 50 μM) was determined from the curve.

Bio-layer interferometry (BLI) binding assays

The binding kinetics of the *NmeHNNH* to different forms of *NmeAcrIIC1* and variants were measured by BLI on a ForteBio Octet RED96 system (Pall ForteBio LLC). Assays were performed at 37 °C in a 96-well black flat bottom plate (Greiner Bio-One) with orbital shaking at 1000 rpm in an assay buffer of 20 mM Tris, 100 mM NaCl, pH 7.4 (with 1 mM DTT for the reduced *AcrIIC1*). Biotinylated *NmeHNNH* was immobilized onto streptavidin biosensors (ForteBio) and incubated with varying concentrations of analytes in the solution. The kinetic experiments comprised 7 steps: (i) baseline acquisition: streptavidin biosensors were incubated in the assay buffer for 2 min; (ii) an auto-inhibition step: the analytes were incubated with the biosensors for 2 min; (iii) second baseline acquisition (6 min); (iv) loading: the biotinylated *NmeHNNH* (10 $\mu\text{g}/\text{mL}$) was loaded onto the surfaces of biosensors until the response value accumulates to 1.2 nm; (v) third baseline acquisition (5 min); (vi) association: incubating biosensors with different concentrations of analytes for 3 min to measure K_{on} ; (vii) dissociation: incubating biosensors with the assay buffer for 5 min to measure K_{off} . The resulting curves were corrected by subtracting the blank reference, then fitted to a global fit algorithm using a 1:1 binding assumption to determine the K_{d} ($K_{\text{off}}/K_{\text{on}}$) by the ForteBio Data Analysis software 9.0.

In vitro transcription and purification of sgRNA

In vitro transcription was carried out with in-house purified T7 RNA polymerase using a standard protocol. The template (dsDNA) for sgRNA was generated by PCR. The sequence of the sgRNA is 5'-GG GUGCGCGCGCAUUAACCUUACGUUGUAGCUCCUUCUCAUUUC GGAACGAAUAGAGAACCGUUGCUACAAUAAGGCCGUCUGAAAAGA UGUGCCGCAACGCUCUGCCCUUAAAGCUU-3'. Transcription reactions were performed at 37 °C for 4 h in buffer containing 0.1 M HEPES-K, 12 mM MgCl_2 , 30 mM DTT, 2 mM spermidine, 2 mM each rNTP (rATP, rUTP, rGTP, rCTP), 100 $\mu\text{g}/\text{mL}$ T7 polymerase, and 500 nM transcription template. The sgRNA was purified using an 8% denatured polyacrylamide gel and then ran through the Elutrap system. Finally, the sgRNA was resuspended in diethylpyrocarbonate (DEPC) H_2O , stored at -80 °C.

In vitro DNA cleavage assays

For 10 μL of the reaction system, 2 μM Cas9 RNP complex (2 μM Cas9 mixed with 2.5 μM sgRNA) was pre-formed in the reaction buffer (20 mM HEPES, pH 7.5, 100 mM KCl, 10 mM MgCl_2 , and 5% (w/v) glycerol with or without 5 mM DTT for reducing condition and oxidizing condition, respectively). About 0–4 μM *AcrIIC1* was added into the system with the molar ratios of Cas9 to *AcrIIC1* ranging from 1:0 to 1:2. The target DNA containing a protospacer sequence with PAM motif (5'-TGCGCGGCGCATTACCTTTACGCCGGATTGCTG-3') was cloned and amplified using PCR. About 400 ng target DNA was added last and the cleavage reaction was performed at 37 °C for 30 min. The cleavage products were treated with 50 $\mu\text{g}/\text{mL}$ proteinase K (Solarbio Life Sciences) at 56 °C for 30 min. Finally, the reaction products were separated and visualized using 1% agarose gels stained with ethidium bromide. For assays shown in Fig. 5d, to mimic the oxidizing condition when experiencing oxidative stress, a fivefold molar ratio of H_2O_2 relative to *AcrIIC1* variants was added. The reaction was performed for 50 min to compensate for the decreased activity of Cas9 potentially caused by H_2O_2 damage.

Structure determination by NMR

We used solution NMR for the structural calculation of the reduced *NmeAcrIIC1*. 100 starting structures of the reduced *NmeAcrIIC1* were initially calculated using CYANA^{46,47} and then refined with AMBER⁴⁸. Only distance restraints obtained from 3D $^{13}\text{C}/^{15}\text{N}$ -edited NOESY-HSQC experiments were used as initial inputs for the first several rounds of calculation in CYANA. In the following iterations, 92 torsion angle restraints for both ϕ and ψ predicted by TALOS+ were included⁴⁹, based on the secondary structure identified from the early structure ensembles. Hydrogen-deuterium exchange experiments were carried out to identify the protected amides and confirm the hydrogen bond network in secondary structures. The chemical shifts for C_α and C_β of C17 and C80 clearly show their reduced states, so we kept them as cysteines along with the structural calculation. The 100 structures with the lowest target functions were refined in AMBER 14.0 using a 20-ps restrained simulated annealing protocol. The annealing was done with the ff14SB force field and generalized Born solvation model, restrained by the same distances and torsion angles used in CYANA with force constants of 35 and 20 $\text{kcal mol}^{-1} \text{\AA}^{-1}$, respectively. In addition, chirality restraints were applied along the main chain to prevent inversions of chirality at high temperatures. The 20 conformers with the lowest AMBER energy were finally selected.

^{15}N backbone relaxation measurements

The backbone ^{15}N relaxation parameters longitudinal relaxation rates R_1 [$1/T_1$], transverse relaxation rates R_2 [$1/T_2$], and steady-state heteronuclear NOEs were measured using standard pulse sequences⁵⁰. Experiments were performed on Bruker Avance 600 MHz NMR spectrometer at 25 °C. Spectral widths of 8417.5 and 1702.9 Hz were used for ^1H and ^{15}N dimensions, respectively. For the T_1 and T_2 measurements, 1024 (^1H) and 128 (^{15}N) complex data points were collected with 16 transients and a recycle delay of 3 s. For the reduced *NmeAcrIIC1*, the delays used for the T_1 experiments were 10 ($\times 2$), 60, 120, 200, 300, 500, 800, 1100, 1500, and 2000 ms, and those used for the T_2 experiments were 10 ($\times 2$), 30, 50, 80, 120, 160, 200, 250, and 300 ms. For the oxidized *NmeAcrIIC1*, the delays used for the T_1 experiments were 10 ($\times 2$), 60, 120, 200, 300, 500, 800, 1100, 1500, 2000, and 2500 ms, and those used for the T_2 experiments were 10 ($\times 2$), 30, 50, 80, 120, 160, 200, and 250 ms. The relaxation rate constants were obtained by fitting the peak intensities to a single exponential function using the nonlinear least squares method. For the $\{^1\text{H}\}$ - ^{15}N Het-NOE measurements, two spectra were performed in the presence and

absence of a 3 s proton pre-saturation period prior to the ^{15}N excitation pulse and using recycle delays of 2 and 5 s, respectively. 32 transients were used for each experiment. Het-NOE values were calculated from the ratio of peak intensities with and without proton saturation. The rotational correlation times values (τ_c) were estimated by the following equation:

$$\tau_c \approx \frac{1}{4\pi\nu_N} \sqrt{6 \frac{R_2}{R_1} - 7} \quad (1)$$

where ν_N is the ^{15}N resonance frequency (in Hz)⁵¹.

Crystal growth, X-ray diffraction, and structural determination

The oxidized *NmeAcrIIc1* was concentrated to 20 mg/mL in buffer 20 mM Tris, pH 7.4, 100 mM NaCl for crystallization. 1 μL protein and 1 μL of reservoir buffer (1.8 M $(\text{NH}_4)_2\text{SO}_4$, 0.1 M Bis-Tris at pH 6.5 and 2% (v/v) polyethylene glycol monomethyl ether 550) were mixed for crystallization at 16 °C in a sitting drop manner. Crystals appear in about one week. Single crystals were immersed in mother liquor containing 20% (v/v) glycerol and flash-frozen in liquid nitrogen. Diffraction data sets were collected at the beamline BL18U1 of the SSRF (Shanghai Synchrotron Radiation Facility)⁵². Data sets were processed with XDS and autoPROC software suite^{53,54}. The structure from PDB entry 5VGB was used as a search template to solve the structure of the oxidized *NmeAcrIIc1* by molecular replacement in the Phenix suite⁵⁵. All structure models were manually adjusted in Coot and refined with Phenix refine program^{55,56}. All the figures of protein structure were prepared with the software PyMol (<http://www.pymol.org>).

pKa determination by NMR

^1H - ^{13}C HSQCs were used to acquire the chemical shifts of C_β for Cys17 and Cys80 during pH titration. NMR sample with gradually increased pH values (6.0, 6.5, 7.0, 7.5, 8.0, 8.5, 9.0, and 9.5) was obtained by buffer exchanging into 50 mM Tris, 100 mM NaCl adjusted at corresponding pH. Chemical shifts were calibrated using DSS (2,2-Dimethyl-2-Silapentane-5-Sulfonic acid), and plotted against the pH values. GraphPad Prism 8 was used to analyze the pH dependence of chemical shifts, the resulting sigmoidal curve was subjected to nonlinear least squares fitting to the modified Henderson-Hasselbalch equation:

$$\delta = \delta_{\text{low}} - \frac{\delta_{\text{low}} - \delta_{\text{high}}}{1 + 10^{n(\text{pK}_a - \text{pH})}} \quad (2)$$

where the pK_a is the ionization constant, δ_{low} is the low pH chemical shift plateau, δ_{high} is the high pH chemical shift plateau, and n is the apparent Hill coefficient⁵⁷.

Antimicrobial susceptibility assays

First, using the two-plasmid CRISPR system pCas-pSG reported by Dr. Quanjian Ji's group²³, we sought to delete the kanamycin resistance gene *kmR* carried with the pSG plasmid in the industrial *E. coli* strain BL21 and verified the genome-editing ability by observing a larger inhibition zone of the bacterial lawn of growth, compared to the negative control carrying no spacer gene. To do this, the pCas plasmid was first transformed into the *E. coli* strain to obtain the pCas-harboring strain, and the cells containing the pCas plasmid were collected and prepared as competent cells. Then, the *kmR* spacer-introduced plasmid pSG-KMR was transformed into the aforementioned pCas-harboring competent cells, and the freshly cultured *E. coli* cells were suspended, diluted, and plated with a kanamycin (100 μg) tablet placed in the center at 30 °C overnight. The diameter of the inhibition ring was measured after 20 h incubation. A control experiment using bacterial cells harboring pSG plasmid without a spacer gene was carried out at the same time. For experimental details, we followed Ji group's publication²³. To make a quantitative comparison

of the size of the inhibition zone, we controlled the amount of the plasmids transformed, the cell turbidity and the culture volume coated, and the incubation time to be precisely consistent among different groups of experiments. Replication of each group of experiments more than three times yields consistent data.

Second, to assess the anti-CRISPR activity of AcrIIc1, the plasmid expressing WT or mutant AcrIIc1 was transformed into the pCas-harboring competent cells and prepared as a new kind of competent cell harboring both pCas and pAcrIIc1 plasmids. Then, the plasmid pSG-KMR or pSG was transformed into the aforementioned pCas-pAcrIIc1-harboring competent cells and the *E. coli* cells were cultured. The expression of AcrIIc1 was induced with 0.5 mM of IPTG when the cell density reached an OD_{600} of 0.2. Then as above, when OD_{600} reached 0.6, the cells were suspended, diluted, and plated. For assays under oxidizing environments, 1 mM H_2O_2 was added along with IPTG to induce the expression of the oxidized AcrIIc1 in the cell.

To confirm the overexpression of AcrIIc1 and its redox state, 1 mL of culture after IPTG induction for 2–3 h was centrifuged, and then the cells were resuspended in 100 μL loading buffer. The AcrIIc1 expression and its redox state were analyzed on a 12% native PAGE gel.

Reporting summary

Further information on research design is available in the Nature Portfolio Reporting Summary linked to this article.

Data availability

All data generated or analyzed in this study are included in the main text or the supplementary materials. Atomic coordinates and NMR data for the reduced *NmeAcrIIc1* have been deposited in the Protein Data Bank (PDB) under entry ID 7X31 and Biological Magnetic Resonance Bank (BMRB) under entry ID 36471. Atomic coordinates and structure factors for the crystal structures of the oxidized state of *NmeAcrIIc1* have been deposited in the PDB under entry ID 7X4B. One other published PDB code cited in this paper is 5VGB. The coordinates for the structural models generated in this study are provided as supporting information. The source data are provided as a Source Data file with this paper. Source data are provided with this paper.

References

- Knott, G. J. & Doudna, J. A. CRISPR-Cas guides the future of genetic engineering. *Science* **361**, 866–869 (2018).
- Hsu, P. D. et al. DNA targeting specificity of RNA-guided Cas9 nucleases. *Nat. Biotechnol.* **31**, 827–832 (2013).
- Pattanayak, V. et al. High-throughput profiling of off-target DNA cleavage reveals RNA-programmed Cas9 nuclease specificity. *Nat. Biotechnol.* **31**, 839–843 (2013).
- Borges, A. L., Davidson, A. R. & Bondy-Denomy, J. The discovery, mechanisms, and evolutionary impact of anti-CRISPRs. *Annu. Rev. Virol.* **4**, 37–59 (2017).
- Stanley, S. Y. & Maxwell, K. L. Phage-encoded anti-CRISPR defenses. *Annu. Rev. Genet.* **52**, 445–464 (2018).
- Marino, N. D., Pinilla-Redondo, R., Csörgő, B. & Bondy-Denomy, J. Anti-CRISPR protein applications: natural brakes for CRISPR-Cas technologies. *Nat. Methods* **17**, 471–479 (2020).
- Davidson, A. R. et al. Anti-CRISPRs: protein inhibitors of CRISPR-Cas systems. *Annu. Rev. Biochem.* **89**, 309–332 (2020).
- Pawluk, A. et al. Naturally occurring off-switches for CRISPR-Cas9. *Cell* **167**, 1829–1838.e9 (2016).
- Bondy-Denomy, J. et al. Multiple mechanisms for CRISPR-Cas inhibition by anti-CRISPR proteins. *Nature* **526**, 136–139 (2015).
- Dong, D. et al. Structural basis of CRISPR–SpyCas9 inhibition by an anti-CRISPR protein. *Nature* **546**, 436–439 (2017).
- Thavalingam, A. et al. Inhibition of CRISPR-Cas9 ribonucleoprotein complex assembly by anti-CRISPR AcrIIc2. *Nat. Commun.* **10**, 2806 (2019).

12. Zhu, Y. et al. Diverse mechanisms of CRISPR-Cas9 inhibition by type IIC anti-CRISPR proteins. *Mol. Cell* **74**, 296–309.e7 (2019).
13. Rauch, B. J. et al. Inhibition of CRISPR-Cas9 with bacteriophage proteins. *Cell* **168**, 150–158.e10 (2017).
14. Harrington, L. B. et al. A broad-spectrum inhibitor of CRISPR-Cas9. *Cell* **170**, 1224–1233.e15 (2017).
15. Mathony, J. et al. Computational design of anti-CRISPR proteins with improved inhibition potency. *Nat. Chem. Biol.* **16**, 725–730 (2020).
16. Hoffmann, M. D. et al. Cell-specific CRISPR-Cas9 activation by microRNA-dependent expression of anti-CRISPR proteins. *Nucleic Acids Res.* **47**, e75 (2019).
17. Martin, O. A., Villegas, M. E., Vila, J. A. & Scheraga, H. A. Analysis of $^{13}\text{C}\alpha$ and $^{13}\text{C}\beta$ chemical shifts of cysteine and cystine residues in proteins: a quantum chemical approach. *J. Biomol. NMR* **46**, 217–225 (2010).
18. Deponte, M. & Horst Lillig, C. Enzymatic control of cysteinyl thiol switches in proteins. *Biol. Chem.* **396**, 401–413 (2015).
19. Lindley, H. A study of the kinetics of the reaction between thiol compounds and chloroacetamide. *Biochem. J.* **74**, 577–584 (1960).
20. Oda, Y. et al. Individual ionization constants of all the carboxyl groups in ribonuclease HI from *Escherichia coli* determined by NMR. *Biochemistry* **33**, 5275–5284 (1994).
21. Jeng, M.-F., Holmgren, A. & Dyson, H. J. Proton sharing between cysteine thiols in *Escherichia coli* thioredoxin: implications for the mechanism of protein disulfide reduction. *Biochemistry* **34**, 10101–10105 (1995).
22. Benjamin Stranges, P. & Kuhlman, B. A comparison of successful and failed protein interface designs highlights the challenges of designing buried hydrogen bonds. *Protein Sci.* **22**, 74–82 (2013).
23. Wang, Y. et al. CRISPR-Cas9 and CRISPR-assisted cytidine deaminase enable precise and efficient genome editing in *Klebsiella pneumoniae*. *Appl. Environ. Microbiol.* **84**, e01834–18 (2018).
24. Ortiz de Oru  Lucana, D., Wedderhoff, I. & Groves, M. R. ROS-mediated signalling in bacteria: zinc-containing Cys-X-X-Cys redox centres and iron-based oxidative stress. *J. Signal Transduct.* **2012**, 605905 (2011).
25. Jumper, J. et al. Highly accurate protein structure prediction with AlphaFold. *Nature* **596**, 583–589 (2021).
26. Bondy-Denomy, J., Pawluk, A., Maxwell, K. L. & Davidson, A. R. Bacteriophage genes that inactivate the CRISPR/Cas bacterial immune system. *Nature* **493**, 429–432 (2013).
27. Kim, Y. et al. Anti-CRISPR AcrIIC3 discriminates between Cas9 orthologs via targeting the variable surface of the HNH nuclease domain. *FEBS J.* **286**, 4661–4674 (2019).
28. Phaneuf, C. R. et al. Ultrasensitive multi-species detection of CRISPR-Cas9 by a portable centrifugal microfluidic platform. *Anal. Methods* **11**, 559–565 (2019).
29. Edraki, A. et al. A compact, high-accuracy Cas9 with a dinucleotide PAM for in vivo genome editing. *Mol. Cell* **73**, 714–726.e4 (2019).
30. Seamon, K. J., Light, Y. K., Saada, E. A., Schoeniger, J. S. & Harmon, B. Versatile high-throughput fluorescence assay for monitoring Cas9 activity. *Anal. Chem.* **90**, 6913–6921 (2018).
31. Rousseau, B. A., Hou, Z., Gramelspacher, M. J. & Zhang, Y. Programmable RNA cleavage and recognition by a natural CRISPR-Cas9 system from *Neisseria meningitidis*. *Mol. Cell* **69**, 906–914.e4 (2018).
32. Go, Y. M. & Jones, D. P. Redox compartmentalization in eukaryotic cells. *Biochim. Biophys. Acta* **1780**, 1273–1290 (2008).
33. Jones, D. P. & Go, Y. M. Redox compartmentalization and cellular stress. *Diabetes Obes. Metab.* **12**, 116–125 (2010).
34. Go, Y. M. & Jones, D. P. Intracellular proatherogenic events and cell adhesion modulated by extracellular thiol/disulfide redox state. *Circulation* **111**, 2973–2980 (2005).
35. Wang, X. et al. Cryptic prophages help bacteria cope with adverse environments. *Nat. Commun.* **1**, 147 (2010).
36. Prasad, S., Gupta, S. C. & Tyagi, A. K. Reactive oxygen species (ROS) and cancer: role of antioxidative nutraceuticals. *Cancer Lett.* **387**, 95–105 (2017).
37. Mok, B. Y. et al. A bacterial cytidine deaminase toxin enables CRISPR-free mitochondrial base editing. *Nature* **583**, 631–637 (2020).
38. Nakamura, M. et al. Anti-CRISPR-mediated control of gene editing and synthetic circuits in eukaryotic cells. *Nat. Commun.* **10**, 194 (2019).
39. Marino, N. D. et al. Discovery of widespread type I and type V CRISPR-Cas inhibitors. *Science* **362**, 240–242 (2018).
40. Bubeck, F. et al. Engineered anti-CRISPR proteins for optogenetic control of CRISPR-Cas9. *Nat. Methods* **15**, 924–927 (2018).
41. Liu, H., Zhu, Y., Lu, Z. & Huang, Z. Structural basis of *Staphylococcus aureus* Cas9 inhibition by AcrIIA14. *Nucleic Acids Res.* **49**, 6587–6595 (2021).
42. Delaglio, F. et al. NMRPipe: a multidimensional spectral processing system based on UNIX pipes. *J. Biomol. NMR* **6**, 277–293 (1995).
43. Vranken, W. F. et al. The CCPN data model for NMR spectroscopy: development of a software pipeline. *Proteins Struct. Funct. Bioinforma.* **59**, 687–696 (2005).
44. Sattler, M., Schleucher, J. & Griesinger, C. Heteronuclear multi-dimensional NMR experiments for the structure determination of proteins in solution employing pulsed field gradients. *Prog. Nucl. Magn. Reson. Spectrosc.* **34**, 93–158 (1999).
45. Stecher, G., Tamura, K. & Kumar, S. Molecular evolutionary genetics analysis (MEGA) for macOS. *Mol. Biol. Evol.* **37**, 1237–1239 (2020).
46. Herrmann, T., G ntert, P. & W thrich, K. Protein NMR structure determination with automated NOE assignment using the new software CANDID and the torsion angle dynamics algorithm DYANA. *J. Mol. Biol.* **319**, 209–227 (2002).
47. G ntert, P., Mumenthaler, C. & W thrich, K. Torsion angle dynamics for NMR structure calculation with the new program DYANA. *J. Mol. Biol.* **273**, 283–298 (1997).
48. Case, D. A. et al. The Amber biomolecular simulation programs. *J. Comput. Chem.* **26**, 1668–1688 (2005).
49. Shen, Y., Delaglio, F., Cornilescu, G. & Bax, A. TALOS+: a hybrid method for predicting protein backbone torsion angles from NMR chemical shifts. *J. Biomol. NMR* **44**, 213–223 (2009).
50. Farrow, N. A. et al. Backbone dynamics of a free and a phosphopeptide-complexed Src homology 2 domain studied by ^{15}N NMR relaxation. *Biochemistry* **33**, 5984–6003 (1994).
51. Kay, L. E., Torchia, D. A. & Bax, A. Backbone dynamics of proteins as studied by ^{15}N inverse detected heteronuclear NMR spectroscopy: application to staphylococcal nuclease. *Biochemistry* **28**, 8972–8979 (1989).
52. Wang, Q. S. et al. The macromolecular crystallography beamline of SSRF. *Nucl. Sci. Tech.* **26**, 12–17 (2015).
53. Kabsch, W. XDS. *Acta Crystallogr. Sect. D. Biol. Crystallogr.* **66**, 125–132 (2010).
54. Vonrhein, C. et al. Data processing and analysis with the autoPROC toolbox. *Acta Crystallogr. D. Biol. Crystallogr.* **67**, 293–302 (2011).
55. Adams, P. D. et al. PHENIX: building new software for automated crystallographic structure determination. *Acta Crystallogr. D. Biol. Crystallogr.* **58**, 1948–1954 (2002).
56. Emsley, P. & Cowtan, K. Coot: model-building tools for molecular graphics. *Acta Crystallogr. D. Biol. Crystallogr.* **60**, 2126–2132 (2004).
57. Jane Dyson, H., Tennant, L. L. & Holmgren, A. Proton-transfer effects in the active-site region of *Escherichia coli* thioredoxin using two-dimensional ^1H NMR. *Biochemistry* **30**, 4262–4268 (1991).

Acknowledgements

We thank Dr. Chunfu Xu for his help on the structural model using AlphaFold and Dr. Qianjiang Ji for generously providing the pCas-pSG plasmids and helpful discussions. We thank Dr. Peter Hsu for his critical reading of the manuscript. We also thank the NMR facility of the National

Center for Protein Sciences at Peking University for assistance with NMR and Dr. Hongwei Li for help with data collection, and the staff members of the National Facility for Protein Science in Shanghai, Zhangjiang Laboratory for providing technical support and assistance in NMR and BLI data collection. This work was supported by the National Natural Science Foundation of China (31900863 to F.Y., joint funds U1932204 to S.Z., and 31800630 to Y.Z.), the Natural Science Foundation of Heilongjiang Province of China (LH2021C049 to F.Y.), the Fundamental Research Funds for the Central Universities (HIT.NSRIF202210 to F.Y.), CAS project for Young Scientists in Basic Research (YSBR-009 to S.Z.), and the funds from the International Cooperation Division at Harbin Institute of Technology.

Author contributions

F.Y. conceived the project, performed the NMR experiments and analysis, and wrote the paper. Y. Zhao, J.H., and S.-S.Y. contributed to the sample preparation, NMR analysis, and in vitro assays. J. Zhong and S.W. performed the DNA cleavage assays. J.L. solved the crystal structure. Y.J., F.J., B.R., Y. Zhu, J. Zhang, and Y.X. helped in the protein purification and binding analysis. R.Z. performed the phylogenetic analysis. J. Zhong, H.C., and F.H. contributed to the antimicrobial susceptibility assays. Z.H., S.Z., and F.Y. supervised the project.

Competing interests

The authors declare no competing interests.

Additional information

Supplementary information The online version contains supplementary material available at <https://doi.org/10.1038/s41467-022-34551-8>.

Correspondence and requests for materials should be addressed to Fan Yang.

Peer review information *Nature Communications* thanks Hyun Ho Park and the other, anonymous, reviewer(s) for their contribution to the peer review of this work. Peer reviewer reports are available.

Reprints and permissions information is available at <http://www.nature.com/reprints>

Publisher's note Springer Nature remains neutral with regard to jurisdictional claims in published maps and institutional affiliations.

Open Access This article is licensed under a Creative Commons Attribution 4.0 International License, which permits use, sharing, adaptation, distribution and reproduction in any medium or format, as long as you give appropriate credit to the original author(s) and the source, provide a link to the Creative Commons license, and indicate if changes were made. The images or other third party material in this article are included in the article's Creative Commons license, unless indicated otherwise in a credit line to the material. If material is not included in the article's Creative Commons license and your intended use is not permitted by statutory regulation or exceeds the permitted use, you will need to obtain permission directly from the copyright holder. To view a copy of this license, visit <http://creativecommons.org/licenses/by/4.0/>.

© The Author(s) 2022